electronics

MDPI

Article

Research on Train Positioning Method Based on Maximum Correntropy Robust Filtering with Dynamic Kernel Bandwidth

Weishu Wang [1], Shanyi Song [1], Cong Peng [2,*] and Dacheng Xu [1]

[1] China Academy of Railway Sciences Corporation Limited, Beijing 100081, China; wangweishu@rails.cn (W.W.); songshanyi@rails.cn (S.S.); xudacheng@rails.cn (D.X.)
[2] School of Automation and Intelligence, Beijing Jiaotong University, Beijing 100044, China
* Correspondence: pengcong@bjtu.edu.cn; Tel.: +86-15611251255

Abstract

Accurate and reliable train positioning is essential for railway operation control systems. However, conventional extended Kalman filter-based solutions are vulnerable to measurement faults, which can significantly degrade positioning performance. To address this issue, this paper proposes an adaptive maximum correntropy robust filter (AMCRF) for a GNSS/INS-based train positioning system. The loss function of the extended Kalman filter is reformulated from the minimum mean square error criterion to a maximumcorrentropy criterion, thereby improving the algorithm's robustness against measurement faults. In AMCRF, considering the limitation of using a fixed kernel bandwidth, a lion swarm optimization strategy is introduced to adaptively tune the kernel bandwidth for each visible satellite, enabling the filter to adapt to time-varying measurement quality and fault magnitudes. By embedding the adaptive mechanism into an extended Kalman filtering framework, the proposed method achieves enhanced fault tolerance. The effectiveness of the proposed AMCRF is validated using experimental data collected along the Qinghai–Tibet Railway. Step and ramp faults of different magnitudes are injected into pseudorange measurements to evaluate fault tolerance. Experimental results demonstrate that the proposed method effectively suppresses the influence of faulty measurements and maintains positioning accuracy close to that under fault-free conditions.

Keywords: train positioning; adaptive robust filtering; maximum correntropy criterion; kernel bandwidth

1. Introduction

Train control systems are safety-critical components that ensure railway operational safety and improve transport efficiency [1]. In China, CTCS-2 and CTCS-3 have been widely deployed and play a key role in supporting large-scale railway operations. However, these systems still largely rely on trackside equipment, such as track circuits and balises, for train localization [2]. This infrastructure-dependent architecture leads to high installation and maintenance costs, particularly on long-distance, low-density railway lines or in complex operating environments where deploying and maintaining conventional trackside equipment is more challenging [3]. Therefore, reducing reliance on trackside infrastructure and developing onboard-centric train positioning technologies have become important directions for next-generation train control systems.

Global Navigation Satellite Systems (GNSS) provide all-weather, real-time, and high-precision positioning capabilities. By enabling accurate position estimation without extensive trackside equipment, GNSS-based solutions can significantly reduce operational

Academic Editor: Ping-Feng Pai

Received: 18 May 2026
Revised: 3 June 2026
Accepted: 4 June 2026
Published: 25 June 2026

costs. Consequently, this technology is gradually being integrated into train control systems worldwide, including Europe's Next Generation Train Control (NGTC) [4], the United States' Positive Train Control (PTC) [5], and China's Train Control System (CTCS) [6]. GNSS is regarded as a key enabling technology for future train positioning systems.

In recent years, many researchers have conducted extensive studies on GNSS-based train positioning from various perspectives. For instance, C. Stallo analyzed the influence of railway-specific environmental factors—such as multipath propagation, foliage attenuation, and signal shadowing—on train positioning performance [7]. Mikhaylov introduced Real-Time Kinematic (RTK) techniques to improve train positioning accuracy, demonstrating that positioning performance degrades significantly due to multipath effects and signal obstruction [8].

Standalone GNSS can achieve high positioning accuracy under favourable observation conditions with sufficient satellite visibility. However, satellite visibility is often severely reduced in challenging environments such as tunnels, mountainous regions, and dense urban areas. Under these conditions, GNSS-only positioning fails to meet the requirements for continuity, reliability, and integrity. To overcome the limitations of a single sensor, multi-sensor fusion techniques have been widely investigated. By incorporating auxiliary information from other sensors—such as LiDAR [9], visual cameras [10], inertial measurement units (IMUs) [11], and odometers [12]—the positioning accuracy and robustness can be effectively improved under GNSS-limited conditions. Wang presented a visual landmark-assisted positioning framework based on LiDAR and inertial navigation, leveraging a kilometer-position plane for trajectory correction [13]. Wang et al. proposed an infrastructure-free train positioning framework using vision and millimeter-wave radar. The radar is employed for train speed estimation, while a loop closure mechanism is introduced to identify the key location for correcting the train position [14]. Both LiDAR and cameras belong to exteroceptive sensing technologies. In exteroceptive sensor fusion approaches, reliable positioning typically depends on the construction of a feature-rich landmark database containing georeferenced railway infrastructure elements, such as panels, signals, and signal gantries [15]. However, the performance of such methods tends to degrade in environments with sparse or featureless surroundings. Given the special operating characteristics of railway systems, dead-reckoning-based sensors are often compatible with railway positioning requirements, such as odometers or inertial navigation systems (INS). INS, as a self-contained navigation system, provides independent position solutions and immunity to jamming and interference, making it a prominent choice [16].

At present, mainstream approaches for information fusion are predominantly based on filtering theory, such as the extended Kalman filter (EKF) and the unscented Kalman filter (UKF). These methods exhibit excellent performance when the measurement noise follows a Gaussian distribution. However, in practical train operations, measurement data are inevitably affected by sensor malfunctions, signal blockages, or external interference, which can significantly degrade data quality and introduce large errors into the observation process [17]. When faulty measurements are directly incorporated into the state estimation framework, the performance may deteriorate or render the positioning results unusable. Therefore, enhancing the fault tolerance of integrated train positioning systems is a key requirement for the deep integration of satellite navigation technology with train control systems.

Fault detection has been recognized as an effective means to improve railway system reliability [18–20]. Within the navigation domain, fault detection is an essential component of the integrity monitoring framework, where statistical hypothesis testing is used to assess the consistency of redundant observations and to identify and exclude faulty measurements. Depending on whether the consistency check incorporates only the current

epoch's observations, receiver autonomous integrity monitoring (RAIM) algorithms are classified into snapshot-based and filtering-based approaches. Snapshot RAIM methods rely solely on measurements from the current epoch, including range comparisons [21], least-squares residuals [22], and maximum solution separation [23]. Among these, the least-squares residual method estimates pseudorange residuals via a least-squares solution and uses the posterior unit-weight variance of the squared residual sum as the test statistic. In the presence of faulty measurements, the test statistic increases significantly, enabling fault detection.

To enhance the ability to detect small faults, the concept of M-estimation has been introduced to construct a weighted residual test statistic [24]. Unlike snapshot RAIM algorithms, filter-based RAIM exploits temporal correlation across multiple epochs via filtering. Kalman filter-based RAIM typically consists of two stages: a global test to determine the presence of faults, followed by a local test to identify and exclude faulty measurements [25]. To further leverage historical data, the autonomous integrity monitoring extension (AIME) algorithm computes test statistics over a sliding window of innovation sequences across multiple epochs, thereby improving the detection capability for slowly growing errors [26]. Moreover, to account for impact of filter tracking errors, the least-squares support vector machine (LS-SVM) has been incorporated into the AIME framework, where predicted innovations rather than instantaneousinnovations are used to construct the test statistic [27]. Additional studies have also explored the influence of detection threshold selection [28] and dynamic model uncertainty [29]. It should be noted that all these fault detection and exclusion (FDE) methods can identify and reject large outliers, but remain incapable of detecting subtle faults below the decision threshold. Moreover, in scenarios with insufficient satellite visibility, excluding satellites may further degrade positioning accuracy [30].

In contrast, robust estimation provides an alternative approach to improving fault tolerance. Rather than precisely identifying the fault source, robust estimation mitigates the influence of outliers on state estimation by adapting the estimation process to the actual distribution of the measurement data. Robust filtering is generally achieved by adopting appropriate loss functions, such as the Huber, Cauchy, or Geman–McClure functions [31]. In integrated navigation systems, Huber-based robust estimation has been widely applied to improve system robustness [32]. However, these methods still assign partial weights to outliers, which may reduce estimation accuracy in the presence of faulty measurements. In recent years, a new filter has been proposed, replacing the minimum mean-square error criterion with the maximum correntropy criterion (MCC) [33]. By exploiting higher-order statistical moments, MCC-based methods maximize the similarity between model output and desired response, thereby effectively suppressing the impact of outliers. Moreover, extensions of MCC-based methods to various nonlinear filters have also been reported [34,35]. Nevertheless, most existing MCC-based algorithms rely on a fixed kernel bandwidth parameter. In practical train positioning scenarios, measurement quality can vary in different epochs, making it difficult to select a single constant bandwidth that remains optimal for outliers of different magnitudes.

To address the above problems, this paper provides a new robust train positioning method. The main innovations of this study can be summarized as follows:

1. A robust extended Kalman filter based on the maximum correntropy criterion is derived, which improves state estimation robustness.
2. A lion swarm optimization strategy is introduced to dynamically adjust the kernel bandwidth for each observed satellite, thereby overcoming the limitations of fixed-bandwidth correntropy-based filtering.

3. Comprehensive comparative experiments are conducted under step and ramp fault scenarios to validate the positioning performance of the proposed adaptive maximum correntropy robust filter.

The remainder of this paper is organized as follows. Section 3 introduces the maximum correntropy extended Kalman filter. Section 4 describes the adaptive kernel bandwidth selection method. Section 5 presents the experimental results and corresponding analysis. Finally, Section 6 concludes this paper.

2. Architecture of the Train Control System

The satellite navigation-based train control system mainly consists of two subsystems: the onboard subsystem and the ground subsystem. Figure 1 illustrates the architecture. The ground subsystem comprises a Radio Block Center (RBC), Temporary Speed Restriction Server (TSRS), Train Control Center (TCC), track circuits, balises, Lineside Electronic Units (LEUs), and a Train Control Maintenance Center (TCMC). The RBC is responsible for transmitting movement authorities and track description information to onboard equipment within its control area through the communication network. The TSRS manages temporary speed restriction commands. Track circuits are used to detect train occupancy on railway sections. The TCC performs track circuit coding and transmits block section status information to the interlocking system. Balises transmit fixed or variable telegrams to the onboard controller, providing temporary track data and correcting train odometry errors. The LEU generates balise telegrams according to information received from ground equipment. The TCMC provides remote maintenance, operational supervision, fault warning, and integrated monitoring functions for the ground components of the train control system.

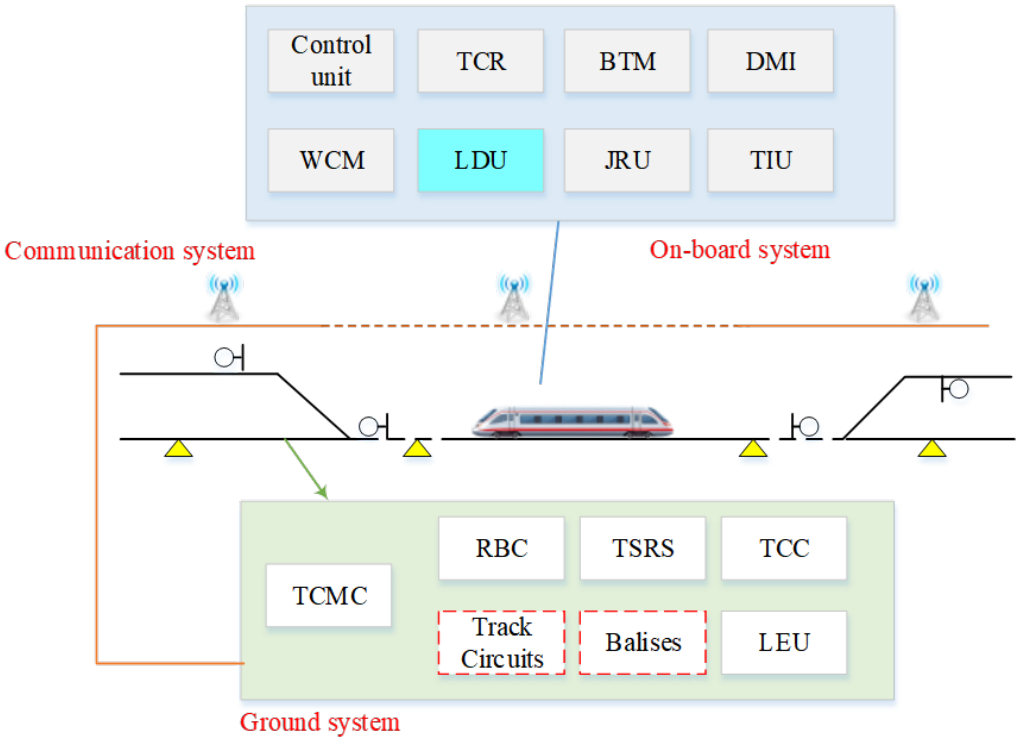

Figure 1. Architecture of the train control system.

The onboard subsystem mainly consists of a control unit, Track Circuit Information Reader (TCR), Balise Transmission Module (BTM), Wireless Communication Module (WCM), Driver–Machine Interface (DMI), Location Determination Unit (LDU), Juridical

Recording Unit (JRU), and Train Interface Unit (TIU) [36]. The onboard subsystem is responsible for continuously monitoring the train's speed and position, generating speed supervision profiles based on information received from the ground subsystem, and automatically initiating braking actions when overspeed conditions or other safety-critical situations are detected [37].

Conventional train positioning methods primarily rely on trackside infrastructure, including balises, and track circuits, to determine train position. In such systems, wheel speed sensors estimate the traveled distance by measuring wheel rotational speed, while balises provide absolute reference position information to correct accumulated odometry errors. In a satellite navigation-based train operation control system, the train positioning function is usually implemented by the Location Determination Unit (LDU). In general, the LDU can be composed of various types of positioning sensors, including GNSS receivers, inertial navigation systems, wheel speed sensors, and other auxiliary sensors. Through multi-sensor information fusion, the limitations of a single sensor in complex railway operating environments can be effectively compensated. Considering the advantages of inertial navigation systems, such as high autonomy, high short-term positioning accuracy, and independence from external signals, this paper mainly focuses on a train positioning architecture based on the integration of satellite navigation and inertial navigation systems.

3. Maximum Correntropy Robust Filtering for Navigation Systems

3.1. Navigation Model

In information fusion, it is first necessary to establish the state and measurement equations of the integrated system. Considering satellite navigation receiver clock bias, clock drift error, as well as the measurement errors of gyroscopes and accelerometers in the inertial navigation system, a 17-dimensional state vector is defined as

$$\mathbf{x} = \begin{bmatrix} \delta\varphi_x & \delta\varphi_y & \delta\varphi_z & \delta v_x & \delta v_y & \delta v_z & \delta x & \delta y & \delta z & \varepsilon_x & \varepsilon_y & \varepsilon_z & \gamma_x & \gamma_y & \gamma_z & b_{clk} & \dot{b}_{clk} \end{bmatrix} \tag{1}$$

In this equation, the ECEF coordinate system is adopted. $(\delta\varphi_x, \delta\varphi_y, \delta\varphi_z)$ represent the attitude errors in three directions, $(\delta v_x, \delta v_y, \delta v_z)$ represent the velocity errors in three directions, $(\delta x, \delta y, \delta z)$ represent the position errors in three directions, $(\varepsilon_x, \varepsilon_y, \varepsilon_z)$ denote the three-axis gyro drift errors, $(\gamma_x, \gamma_y, \gamma_z)$ denote the three-axis accelerometer random errors, b_{clk} corresponds to the equivalent clock bias error, and $\dot{b}_{clk}$ is the equivalent clock drift error.

Furthermore, by combining the error equations of the inertial navigation system and the satellite navigation system, the state equation of the integrated system can be formulated as:

$$\mathbf{x}_k = \mathbf{F}_{k-1}\mathbf{x}_{k-1} + \mathbf{w}_{k-1}, \tag{2}$$

where $\mathbf{F}_{k-1}$ denotes the state transition matrix, which is composed of the error propagation models of GNSS and INS at epoch k. The process noise $\mathbf{w}_{k-1}$ is assumed to follow a zero-mean Gaussian distribution, with the corresponding covariance matrix denoted as $\mathbf{Q}_k$.

Then, considering pseudorange measurements from the satellite navigation receiver and the corresponding predicted pseudoranges derived from the inertial navigation system, the measurement vector can be determined as:

$$\mathbf{z}_k = \boldsymbol{\rho}_{\text{GNSS}} - \boldsymbol{\rho}_{\text{INS}}. \tag{3}$$

The measurement equation of the integrated system can be expressed as:

$$\mathbf{z}_k = \mathbf{H}_k\mathbf{x}_k + \mathbf{v}_k, \tag{4}$$

where $\mathbf{H}_k$ denotes the measurement matrix of the integrated system, and $\mathbf{v}_k$ represents the measurement noise, which is assumed to follow a zero-mean Gaussian distribution with covariance matrix $\mathbf{R}_k$.

3.2. Maximum Correntropy Criterion

Correntropy is a generalized similarity measure between two random variables. For random variables X and Y, the correntropy is defined as

$$V(X,Y) = \mathbb{E}[\varphi(X,Y)] = \iint \varphi(x,y)\, dF_{X,Y}(x,y), \tag{5}$$

where $\mathbb{E}[\cdot]$ denotes the expectation operator, $F_{X,Y}(x,y)$ is the joint probability distribution function of the given random variables, and $\varphi(\cdot)$ is a kernel function, typically chosen as the Gaussian function, defined as:

$$\varphi(X,Y) = G_\lambda(e) = \exp\left(-\frac{e^2}{2\lambda^2}\right), \tag{6}$$

where λ represents the kernel bandwidth, and $e = x - y$.

By expanding the Gaussian function using the Taylor series, the correntropy can be expressed as

$$V(X,Y) = \sum_{n=0}^{\infty} \frac{(-1)^n}{2^n \lambda^{2n} n!} \mathbb{E}\left[(X-Y)^{2n}\right]. \tag{7}$$

It is noteworthy that correntropy represents a weighted sum of all the higher-order moments of the random variables. These higher-order statistical moments significantly enhance the robustness against non-Gaussian noise. Moreover, the kernel bandwidth is a critical free parameter that determines the weighting of the second-order and higher-order moments.

In general, the joint distribution of random variables X and Y is unknown, and the number of available samples is limited. Under these circumstances, the correntropy value can be estimated by averaging over N samples as follows:

$$\hat{V}(X,Y) = \frac{1}{N} \sum_{i=1}^{N} G_\lambda(e(i)), \tag{8}$$

where $e(i) = x(i) - y(i)$. When $x = y$, the correntropy reaches its maximum. This indicates that the larger the correntropy value, the closer the two variables become. Therefore, the maximum correntropy criterion (MCC) can be expressed as:

$$J_{\mathrm{MCC}} = \frac{1}{N} \sum_{i=1}^{N} G_\lambda(e(i)). \tag{9}$$

The optimal solution can be obtained by maximizing this criterion:

$$\hat{\mathbf{W}} = \arg\max_{\mathbf{W}\in\Omega} \frac{1}{N} \sum_{i=1}^{N} G_\lambda(e(i)), \tag{10}$$

where Ω denotes the feasible solution set.

3.3. Maximum Correntropy Robust Filter

The state prediction error, defined as the difference between the true state and the predicted prior state, can be expressed as:

$$\boldsymbol{\eta}_k = \mathbf{x}_k - \hat{\mathbf{x}}_{k|k-1}. \tag{11}$$

Combining the state equation and the measurement equation, the following linear regression model can be obtained:

$$\begin{bmatrix} \hat{\mathbf{x}}_{k|k-1} \\ \mathbf{z}_k \end{bmatrix} = \begin{bmatrix} \mathbf{I} \\ \mathbf{H}_k \end{bmatrix} \mathbf{x}_k + \boldsymbol{\alpha}_k, \tag{12}$$

where $\mathbf{I}$ denotes the identity matrix, and

$$\boldsymbol{\alpha}_k = \begin{bmatrix} -\boldsymbol{\eta}_k \\ \mathbf{v}_k \end{bmatrix}. \tag{13}$$

$$\begin{aligned} \mathrm{E}\left[\boldsymbol{\alpha}_k \boldsymbol{\alpha}_k^T\right] &= \begin{bmatrix} \mathbf{P}_{k|k-1} & \mathbf{0} \\ \mathbf{0} & \mathbf{R}_k \end{bmatrix} \\ &= \begin{bmatrix} \mathbf{S}_{P,k|k-1}\mathbf{S}_{P,k|k-1}^T & \mathbf{0} \\ \mathbf{0} & \mathbf{S}_{R,k}\mathbf{S}_{R,k}^T \end{bmatrix}. \\ &= \mathbf{S}_k \mathbf{S}_k^T \end{aligned} \tag{14}$$

where $\mathbf{S}_k$ can be obtained by Cholesky decomposition of $\mathrm{E}\left[\boldsymbol{\alpha}_k \boldsymbol{\alpha}_k^T\right]$.

Multiplying Equation (12) from the left by $\mathbf{S}_k^{-1}$, the linear regression model can be reformulated as

$$\mathbf{L}_k = \boldsymbol{\Gamma}_k \mathbf{x}_k + \boldsymbol{\delta}_k, \tag{15}$$

where $\mathbf{L}_k$, $\boldsymbol{\Gamma}_k$, and $\boldsymbol{\delta}_k$ are respectively defined as

$$\mathbf{L}_k = \mathbf{S}_k^{-1} \begin{bmatrix} \hat{\mathbf{x}}_{k|k-1} \\ \mathbf{z}_k \end{bmatrix}, \tag{16}$$

$$\boldsymbol{\Gamma}_k = \mathbf{S}_k^{-1} \begin{bmatrix} \mathbf{I} \\ \mathbf{H}_k \end{bmatrix}, \tag{17}$$

and

$$\boldsymbol{\delta}_k = \mathbf{S}_k^{-1} \begin{bmatrix} -\boldsymbol{\eta}_k \\ \mathbf{v}_k \end{bmatrix}. \tag{18}$$

To enhance algorithm robustness, the maximum correntropy criterion is introduced as a new loss function:

$$J_{\mathrm{MCC}}(\mathbf{x}_k) = \frac{1}{L} \sum_{i=1}^{L} G_\lambda(\delta_k(i)), \tag{19}$$

Based on the maximum correntropy criterion, the optimal state estimation solution can be obtained by maximizing the following optimization criterion:

$$\hat{\mathbf{x}}_k = \arg\max_{\mathbf{x}_k} \sum_{i=1}^{L} G_\lambda(\delta_k(i)). \tag{20}$$

where $L = m + n$, with m and n denoting the dimensions of the state vector and the measurement vector, respectively. The residual $\delta_k(i)$ denotes the i-th component of $\mathbf{L}_k - \mathbf{\Gamma}_k \mathbf{x}_k$.

Taking the derivative with respect to $\mathbf{x}_k$, we have

$$\frac{\partial J_{\mathrm{MCC}}(\mathbf{x}_k)}{\partial \mathbf{x}_k} = \sum_{i=1}^{L} G_\lambda(\delta_k(i))\delta_k(i)\frac{\partial \delta_k(i)}{\partial \mathbf{x}_k} = 0. \tag{21}$$

Defining $C_k(i) = G_\lambda(\delta_k(i))$, we obtain

$$\mathbf{C}_k = \mathrm{diag}(C_k(1), C_k(2), \ldots, C_k(L)) = \begin{bmatrix} \mathbf{C}_{P,k} & \mathbf{0} \\ \mathbf{0} & \mathbf{C}_{R,k} \end{bmatrix}, \tag{22}$$

where

$$\mathbf{C}_{P,k} = \mathrm{diag}(G_\lambda(\delta_k(1)), G_\lambda(\delta_k(2)), \ldots, G_\lambda(\delta_k(m))), \tag{23}$$

and

$$\mathbf{C}_{R,k} = \mathrm{diag}(G_\lambda(\delta_k(m+1)), G_\lambda(\delta_k(m+2)), \ldots, G_\lambda(\delta_k(L))). \tag{24}$$

Here, $\mathrm{diag}(\cdot)$ indicates the operation of constructing a diagonal matrix. Therefore, Equation (21) can be rewritten as

$$\mathbf{\Gamma}_k^T \mathbf{C}_k (\mathbf{L}_k - \mathbf{\Gamma}_k \mathbf{x}_k) = \mathbf{0}. \tag{25}$$

Expanding Equation (25), we have

$$\mathbf{\Gamma}_\mathbf{k}^\mathbf{T} \mathbf{C}_\mathbf{k} \mathbf{L}_\mathbf{k} - \mathbf{\Gamma}_\mathbf{k}^\mathbf{T} \mathbf{C}_\mathbf{k} \mathbf{\Gamma}_\mathbf{k} \mathbf{x}_\mathbf{k} = \mathbf{0}. \tag{26}$$

Thus, the state vector satisfies

$$\mathbf{\Gamma}_k^T \mathbf{C}_k \mathbf{L}_k = \mathbf{\Gamma}_k^T \mathbf{C}_k \mathbf{\Gamma}_k \mathbf{x}_k. \tag{27}$$

The state at time k can be estimated as

$$\hat{\mathbf{x}}_k = \left(\mathbf{\Gamma}_k^T \mathbf{C}_k \mathbf{\Gamma}_k\right)^{-1} \mathbf{\Gamma}_k^T \mathbf{C}_k \mathbf{L}_k. \tag{28}$$

However, $\mathbf{C}_k$ is determined by the Gaussian kernel function of the residual $\delta_k = \mathbf{L}_\mathbf{k} - \mathbf{\Gamma}_\mathbf{k} \mathbf{x}_\mathbf{k}$, depending on the unknown state $\mathbf{x}_k$. As a result, the above equation is nonlinear with respect to $\mathbf{x}_k$, and cannot be solved directly. To address this issue, a fixed-point iteration strategy is adopted. The iteration continues until the difference between consecutive estimates satisfies a predefined convergence threshold. The convergence threshold is usually set to 10^{-6}.

The weighting matrix $\mathbf{C}_k$ reweights the prior error covariance matrix and reconstructs the measurement noise covariance matrix. The updated covariance matrix is expressed as

$$\mathbf{\Psi}_k = \mathbf{S}_k \mathbf{C}_k^{-1} \mathbf{S}_k^T = \begin{bmatrix} \tilde{\mathbf{P}}_{k|k-1} & \mathbf{0} \\ \mathbf{0} & \tilde{\mathbf{R}}_k \end{bmatrix}. \tag{29}$$

In practice, since the true state is unknown, the estimator is assumed to be unbiased, namely $\hat{\mathbf{x}}_{k|k-1} \approx \mathbf{x}_k$. Thus, $\mathbf{C}_{P,k}$ can be approximated by the identity matrix, simplifying the prior error covariance and measurement noise covariance as

$$\tilde{\mathbf{P}}_{k|k-1} = \mathbf{S}_{P,k|k-1} \mathbf{I} \mathbf{S}_{P,k|k-1}^T = \mathbf{P}_{k|k-1}, \tag{30}$$

and

$$\tilde{\mathbf{R}}_k = \mathbf{S}_{R,k}\mathbf{C}_{R,k}^{-1}\mathbf{S}_{R,k}^T. \tag{31}$$

Finally, the updated covariance matrices are incorporated into the measurement update process to compute the Kalman gain matrix, posterior state estimate, and posterior error covariance matrix:

$$\tilde{\mathbf{K}}_k = \mathbf{P}_{k|k-1}\mathbf{H}_k^T\left(\mathbf{H}_k\mathbf{P}_{k|k-1}\mathbf{H}_k^T + \tilde{\mathbf{R}}_k\right)^{-1}, \tag{32}$$

$$\hat{\mathbf{x}}_k = \hat{\mathbf{x}}_{k|k-1} + \tilde{\mathbf{K}}_k\left(\mathbf{z}_k - \mathbf{H}_k\hat{\mathbf{x}}_{k|k-1}\right), \tag{33}$$

and

$$\mathbf{P}_k = \left(\mathbf{I} - \tilde{\mathbf{K}}_k\mathbf{H}_k\right)\mathbf{P}_{k|k-1}. \tag{34}$$

4. Adaptive Kernel Bandwidth Selection

The kernel bandwidth is a free parameter in the maximum correntropy robust filter and plays a crucial role in determining the robustness of the filter estimation. The choice of kernel bandwidth governs the contribution of prior information and measurement information in the posterior state estimation. An inappropriate selection may prevent the Gaussian kernel function from fully exploiting its capability to suppress the influence of abnormal measurements.

To address this issue, noting that the purpose of kernel bandwidth selection is to minimize the estimation error under fault conditions, the bandwidth selection problem is reformulated as a multivariate single-objective optimization problem. Then, the kernel bandwidths of different satellites are treated as variables, and the optimal set of bandwidths is then determined by solving the constrained optimization problem to minimize the estimation error. The lion swarm optimization (LSO) algorithm, a representative swarm-intelligence optimization method, is incorporated into the robust filtering framework to obtain the optimal kernel bandwidth combination.

4.1. Population Initialization

The primary purpose of population initialization is to define the total number of lions within the population, the quantity of lions in each category, and their initial positions. Due to the distinct roles within the lion swarm, the proportion of adult lions directly influences the algorithm's optimization performance, while the number of lion cubs enhances population diversity and extends the search range.

Assume that the total number of lions is denoted by N, and N_{Adult} denotes the number of adult lions. Their relationship is expressed as

$$N_{\text{Adult}} = \beta N, \tag{35}$$

where β is the proportion factor of adult lions, whose value affects the search efficiency. Typically, β is set to 0.5 to ensure rapid convergence. Correspondingly, the number of lion cubs is $N - N_{\text{Adult}}$. Among adult lions, there is only one lion king, and the remaining adult lions are lionesses.

The position of each lion represents a feasible solution in the optimization space, corresponding to the kernel bandwidth parameters associated for each observed satellite at epoch k. The dimension D is determined by the number of observed satellites. The position of the i-th lion can be represented as

$$\mathbf{p}_i = (p_{i1}, p_{i2}, \ldots, p_{iD}), \quad 1 \le i \le N. \tag{36}$$

After initialization, the positions of all lions within the population can be collectively represented as

$$\mathbf{P} = \begin{bmatrix} p_{11} & p_{12} & \cdots & p_{1D} \\ p_{21} & p_{22} & \cdots & p_{2D} \\ \vdots & \vdots & \ddots & \vdots \\ p_{N1} & p_{N2} & \cdots & p_{ND} \end{bmatrix}. \tag{37}$$

4.2. Fitness Assessment

Before applying the LSO algorithm to determine the kernel bandwidths associated with different observations, it is essential to first define the optimization objective, namely the fitness function. In this study, the fitness function is defined as the horizontal uncertainty level (HUL) of the state estimation. The HUL evaluates the real-time positioning performance of a train based on observational data without a ground-truth position reference [38]. It is expressed as

$$HUL = \max(Slope_i \sigma_i) \sqrt{phais} + K(P_{md}) d_H. \tag{38}$$

$$d_H = \sqrt{\mathbf{P}_{ee} + \mathbf{P}_{nn}}. \tag{39}$$

$$phais = \Delta \mathbf{z}_k^T \mathbf{S}_k^{-1} \Delta \mathbf{z}_k. \tag{40}$$

$$Slope_i = \sqrt{\frac{\mathbf{f}_i^T \mathbf{K}_k^T \boldsymbol{\nu}_e^T \boldsymbol{\nu}_e \mathbf{K}_k \mathbf{f}_i + \mathbf{f}_i^T \mathbf{K}_k^T \boldsymbol{\nu}_n^T \boldsymbol{\nu}_n \mathbf{K}_k \mathbf{f}_i}{\mathbf{f}_i^T \mathbf{S}_k^{-1} \mathbf{f}_\mathbf{i}}}. \tag{41}$$

where σ_i is the standard deviation of the measurement error for the i-th satellite, $Slope_i$ denotes the characteristic slope of the i-th satellite, $\boldsymbol{\nu}$ denotes the target state selected from the full state vector, and $\mathbf{f_i}$ refers to the selected satellite that is to be evaluated, all elements are zero except for those corresponding to the i-th satellite. $\Delta \mathbf{z}_k$ represents the filtering innovation, $\mathbf{S}_k$ denotes the innovation covariance matrix, d_H denotes the horizontal standard deviation of the state estimation. $\mathbf{P}_{\text{ee}}$ and $\mathbf{P}_{nn}$ are the position variances in the east and north directions. $K(P_{md})$ denotes the inflation factor associated with the predefined missed-detection probability, which is obtained in the corresponding chi-square distribution. P_{md} is typically set to 0.01 [25].

The fitness value $f_i(\text{HUL})$ at each iteration is computed based on the current position $\mathbf{p}_i$ of each lion. After a finite number of iterations, the historical optimal position of the lion swarm is obtained, yielding the final feasible solution:

$$\mathbf{p}_{\text{best}} = \arg\min_{\mathbf{p}_i} f_i(HUL). \tag{42}$$

4.3. Lion Swarm Location Update

During the hunting process of the lion swarm, the search direction and scope of each individual are governed by their respective roles within the group. Through collaborative interactions among the lion king, lionesses, and cub lions, the positions of all lions are iteratively updated to approach the optimal solution.

4.3.1. Lion King Position Update

The lion king represents the individual with the best fitness in the population. It guides the migration of the entire group and occupies the optimal position within the swarm. To preserve its leadership status, the lion king only moves within a limited area

around the current optimal position, seeking potentially superior solutions in its vicinity. The position of the lion king at iteration $L+1$ is then updated according to

$$\mathbf{p}_i^{L+1} = \mathbf{g}^L\left(1+\gamma\left\|\mathbf{r}_i^L - \mathbf{g}^L\right\|\right), 0<\gamma<1, \tag{43}$$

where the historical best position of the i-th lion is denoted as $\mathbf{r}_i^L$, $\mathbf{g}^L$ represents the global optimal position, namely the lion king's position, at the L-th iteration, and γ denotes the scaling factor governing the movement range of the lion king. It is typically generated as a random number following a normal distribution.

4.3.2. Lioness Position Update

Lionesses carry the primary responsibility for hunting within the lion swarm. During hunting, lionesses exchange local information and collaboratively search for and surround prey. The position updating of each lioness is influenced by the positions of other lionesses within the swarm. The updated position of the lioness at iteration $L+1$ can be expressed as

$$\mathbf{p}_i^{L+1} = \frac{\mathbf{r}_i^L + \mathbf{p}_c^L}{2}(1+\alpha_h\gamma). \tag{44}$$

where $\mathbf{p_c^L}$ represents the historical best position of another randomly selected lioness, and α_h is the scaling factor governing the movement range of the lioness, determining both the step size and the search speed. The scaling factor progressively decreases with each iteration, causing the lioness's step size to diminish gradually until it eventually approaches zero. The relationship between the scaling factor, step size, and iteration number is expressed as follows:

$$\alpha_h = step \cdot \exp\left(-\frac{30L}{L_a}\right)^{10}. \tag{45}$$

$$step = 0.1\left(\overline{high} - \overline{low}\right). \tag{46}$$

where L_a denotes the total number of iterations, and $step$ represents the lioness's movement step size, calculated using the mean of the maximum and minimum values in each dimension of the search space, denoted as $\overline{high}$ and $\overline{low}$.

4.3.3. Cub Lions Position Updating

Cub lions are the weakest individuals in the population, and their behaviours are mainly influenced by interactions with the lion king and lionesses. To simulate this behaviour, cub lions are divided into three categories using a random variable q^f, which follows a uniform distribution. Each category corresponds to a distinct behavioural pattern.

When $0 < q^f < 1/3$, the cub lion is considered to be in a hungry state. This behaviour manifests as local exploitation around the current global best position.

When $1/3 \le q^f < 2/3$, the cub lion follows a lioness to learn hunting techniques and participate in cooperative hunting. In the solution space, this behaviour corresponds to local exploration around the position of a lioness.

When $2/3 \le q^f < 1$, the cub lion exhibits elite reverse learning behaviour and is expelled to a distant region away from the lion king's domain. The cub lion must survive independently and search for better food sources. In the search space, this behaviour reflects exploration of potential superior solutions far from the current global optimum.

This behavioural strategy enhances the randomness of the search process and increases directional diversity in population movement, effectively reducing the risk of premature

convergence to local optima. Based on the above behaviour classifications, the position of a cub lion at iteration $L+1$ can be updated as follows:

$$\mathbf{p}_i^{L+1} = \begin{cases} \frac{\mathbf{g}^L + \mathbf{r}_i^L}{2}\left(1+\alpha^f\gamma\right), 0 < q^f < \frac{1}{3} \\ \frac{\mathbf{r}_m^L + \mathbf{r}_i^L}{2}\left(1+\alpha^f\gamma\right), \frac{1}{3} \le q^f < \frac{2}{3} \\ \frac{\bar{\mathbf{g}}^L + \mathbf{r}_i^L}{2}\left(1+\alpha^f\gamma\right), \frac{2}{3} \le q^f < 1 \end{cases} \tag{47}$$

where $\mathbf{r}_m^L$ represents the historical best position of the cub lion following the lioness at iteration L, and $\bar{\mathbf{g}}^L$ denotes the expelled position of the i-th cub lion, defined as

$$\bar{\mathbf{g}}^L = \overline{high} + \overline{low} - \mathbf{g}^L. \tag{48}$$

$$\alpha^f = step \cdot \frac{L_a - L}{L_a}. \tag{49}$$

where α^f is a scaling factor that restricts the movement capability of cub lions by scaling down their movement step size according to the iteration number. Initially, cub lions have limited knowledge of the search space and therefore employ relatively large step sizes to facilitate broad exploratory searches. As the optimization process proceeds and the cub lions acquire information about promising regions, the step size is gradually decreased, enabling more focused and localized searches around candidate solutions.

4.4. Boundary Constraint

Boundary constraints are imposed to restrict the feasible solution space of each optimization variable, thereby preventing variables from exceeding their permissible ranges during the optimization process. These ranges are defined by specifying corresponding lower and upper bounds. After the positions of all lions are updated, boundary checks are performed to verify the updated positions. If the value of any variable in a given dimension exceeds the predetermined upper bound, it is set to the upper-bound value:

$$p_{id} = \begin{cases} u_{\text{Bound}}, & p_{id} > u_{\text{Bound}}, \\ l_{\text{Bound}}, & p_{id} < l_{\text{Bound}}, \\ p_{id}, & l_{\text{Bound}} \le p_{id} \le u_{\text{Bound}}, \end{cases} \tag{50}$$

where p_{id} denotes the i-th dimensional variable of the d-th lion's position, while u_{Bound} and l_{Bound} represent the upper and lower boundary values, respectively. The specific boundary values are determined according to the characteristics of the variables. Specifically, an excessively large kernel bandwidth could weaken the robustness of the algorithm, causing the estimation performance to approach that of the conventional EKF. Therefore, an upper boundary value of 10 is chosen in this study. Conversely, an excessively small kernel bandwidth may result in a singular or nearly singular matrix, leading to inaccurate estimation results. To avoid this issue, the lower boundary value is set to 2 [39].

Figure 2 shows the flowchart of the proposed adaptive maximum correntropy robust filter for the GNSS/INS-based train positioning system.

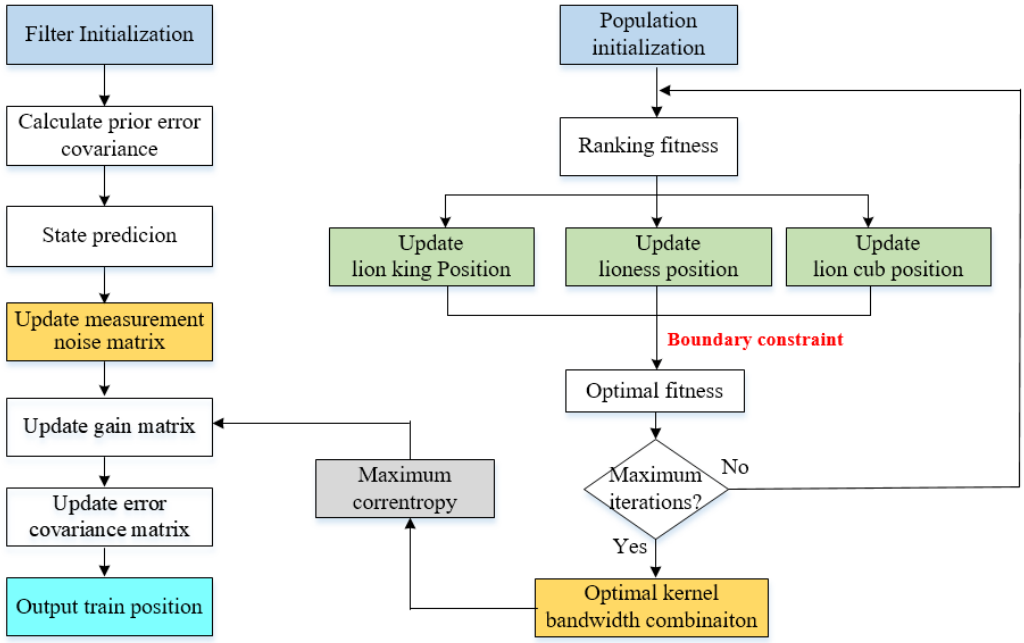

Figure 2. Flowchart of the AMCRF method.

5. Experimental Results

5.1. Experiment Description

To validate the proposed algorithm, simulation experiments were conducted using measurement data collected from the Qinghai–Tibet Railway in western China, which represents a critical application scenario for satellite navigation-based train control systems. The data employed in this study were collected along the Geermu–Yinmaxia section of the Qinghai–Tibet Railway. This section is mainly characterized by open-sky and open-terrain conditions.

The experimental data were collected using a NovAtel SPAN-FSAS integrated navigation system, consisting of a satellite navigation receiver and an inertial measurement unit. According to the manufacturer's specifications, the system can achieve centimeter-level positioning accuracy under high-precision GNSS correction modes. This accuracy level is sufficient for the present fault-injection experiment because the positioning error caused by the faulty pseudorange is at the meter level. The raw satellite observation data were sampled at 1 Hz, and the navigation outputs from the SPAN-FSAS system were used as the ground truth for computing positioning errors. Figures 3 and 4 illustrate the data collection route and the experimental equipment configuration, respectively. During the experiments, the train operated at speeds ranging from 34 km/h to 73 km/h. Satellite visibility remained good throughout the journey, with an average of approximately 10 visible satellites, as shown in Figure 5.

In the LSO-based adaptive kernel bandwidth selection, the maximum number of iterations was set to 50. The iteration number was selected by considering both optimization performance and computational efficiency. A larger iteration number increases the computational burden at each filtering epoch. In the present experiment, the search range is bounded within (2, 10). The selected iteration number provides a sufficient search capability to obtain a stable bandwidth combination while maintaining an acceptable computational cost.

To evaluate the robustness of the proposed AMCRF, step faults and ramp faults with varying magnitudes were injected into the raw pseudorange measurements for positioning performance analysis. Three filtering methods were selected for comparison: the EKF, the MCRF with fixed kernel bandwidths, and the proposed AMCRF. In the MCRF, fixed kernel bandwidths of 3, 5, and 10 were selected to examine the influence of kernel bandwidth on filtering robustness and to compare with the adaptive strategy adopted in AMCRF. To quantitatively evaluate the positioning performance of different algorithms, the root mean square error (RMSE) and the maximum horizontal position error (MHPE) were adopted as performance metrics.

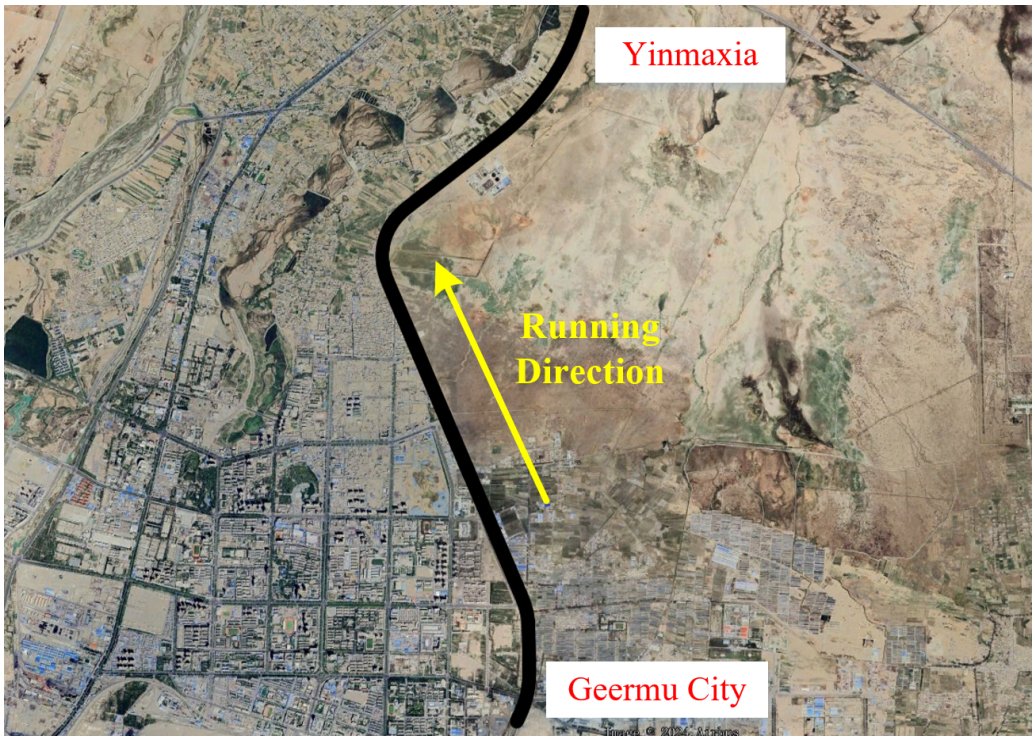

Figure 3. Experimental route.

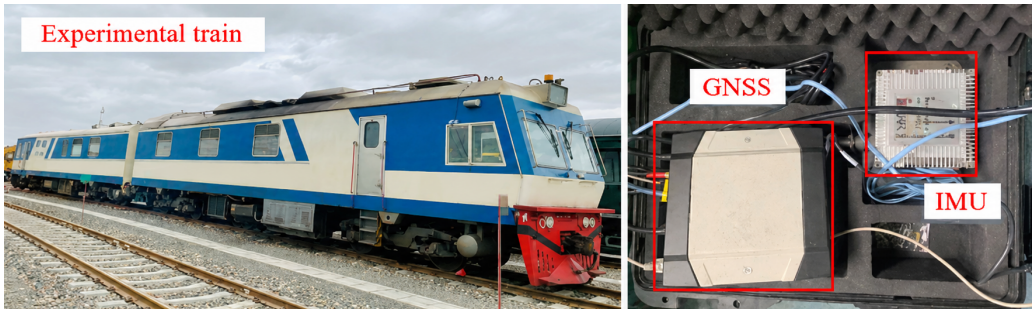

Figure 4. Experimental devices.

5.2. Step Faults

In the step fault scenario, step errors of 15 m, 25 m, and 35 m were injected into the pseudorange measurements of satellite PRN7 at 150 s, 300 s, and 450 s, respectively. Each fault persisted for 50 s. Figure 6 illustrates the evolution of horizontal position errors for different algorithms. Distinct differences in positioning performance can be observed across the three fault regions. The EKF exhibited the highest sensitivity to measurement faults, showing pronounced degradation in positioning accuracy in all fault regions. As the fault magnitude increased, the maximum horizontal positioning error increased accordingly, reaching 2.28 m, 3.13 m, and 3.23 m in Zones 1, 2, and 3, respectively.

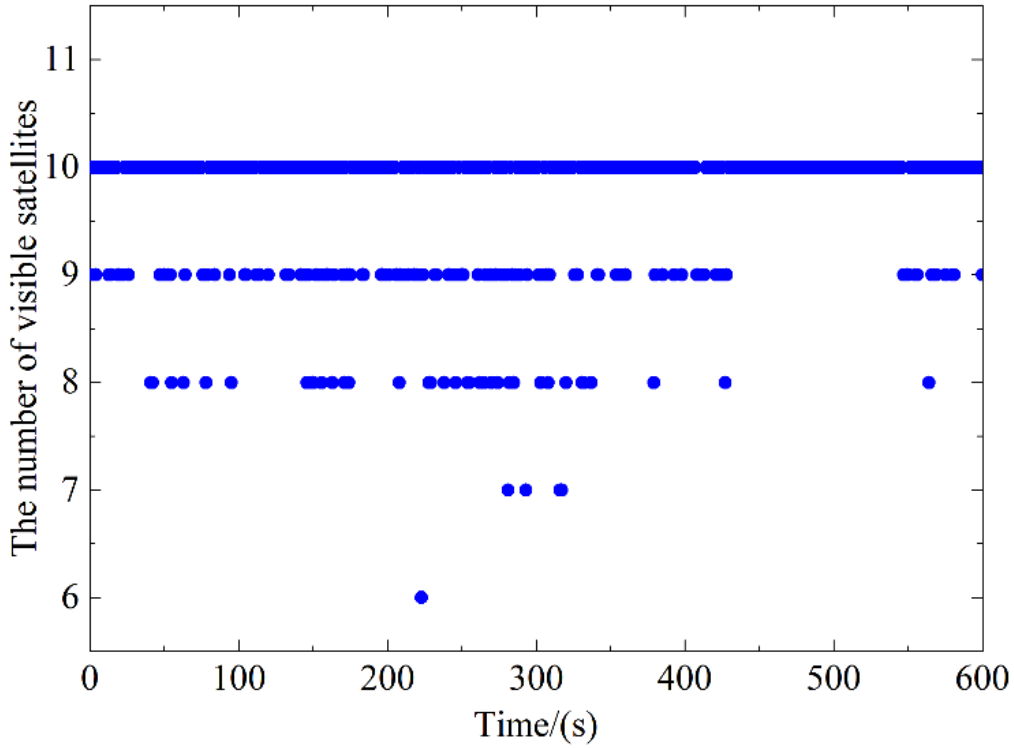

Figure 5. Number of visible satellites.

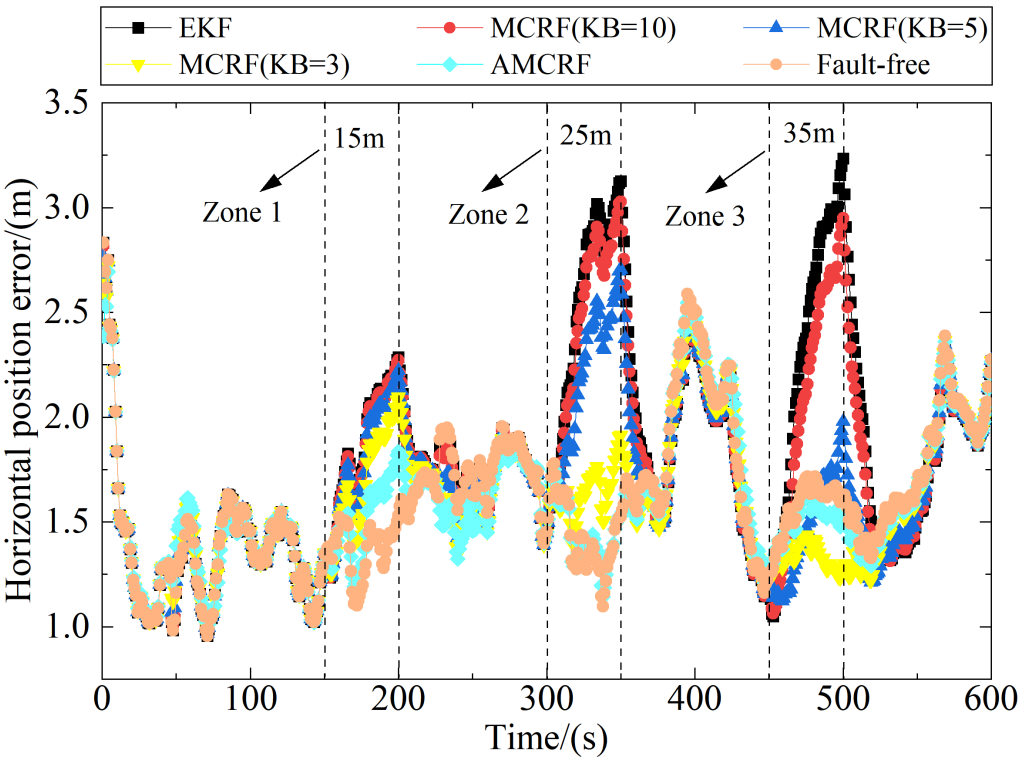

Figure 6. Robustness comparison under different step faults.

Compared with the EKF, the MCRF algorithm exhibited varying levels of fault suppression across different fault regions, depending on the selected kernel bandwidth. Under the same fault magnitude, the robustness of MCRF decreased as the kernel bandwidth increased, resulting in larger positioning errors that became comparable to those of the EKF. When the fault magnitude was 15 m, MCRF showed similar maximum positioning errors under different bandwidth settings, indicating limited fault suppression capability in the presence of small-magnitude faults. However, for a fixed kernel bandwidth, the robustness of MCRF improved as the fault magnitude increased. For instance, when the kernel bandwidth was set to 5, the positioning performance in Zone 1 was comparable to that of the EKF, while the maximum error in Zone 2 was 2.7 m. As the fault magnitude increased to 35 m, the maximum horizontal positioning error estimated by MCRF significantly decreased to 1.98 m.

In contrast, the proposed AMCRF consistently exhibited superior positioning performance in Zones 2 and 3, effectively mitigating the influence of faulty measurements. The positioning accuracy remained close to that under fault-free conditions, which can be attributed to the adaptive kernel bandwidth mechanism that dynamically adjusts the bandwidth for each observed satellite and enables an appropriate parameter configuration. Although the estimation error of AMCRF slightly increased when the fault magnitude was reduced to 15 m, it still outperformed both EKF and MCRF across all scenarios. As shown in Figure 7, the kernel bandwidths associated with different visible satellites varied dynamically within the range of $[2, 10]$, providing greater flexibility than the fixed-bandwidth strategy.

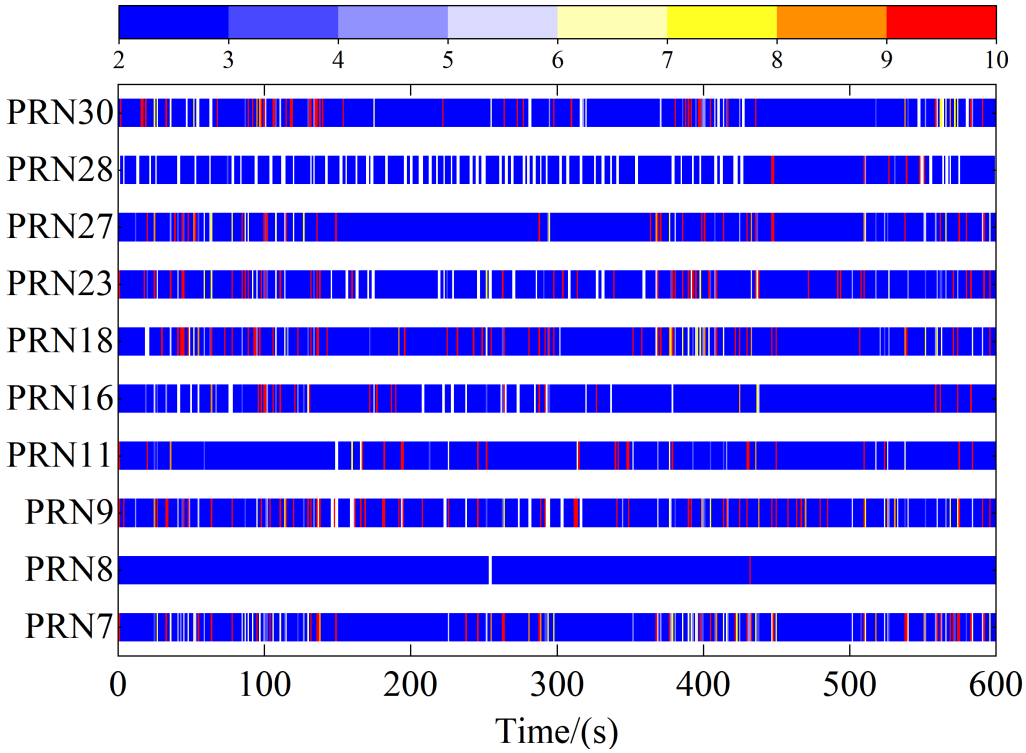

Figure 7. Variation of kernel bandwidths in AMCRF under step faults.

To further quantify the positioning performance, detailed statistical results are summarized in Table 1. Taking Zone 2 as an example, the RMSE of AMCRF was 1.45 m, which is nearly identical to the positioning error under fault-free conditions. Compared with the EKF and the MCRF with fixed kernel bandwidths of 10, 5, and 3, the RMSE was reduced by 42.9%, 40.8%, 33.8%, and 12.1%, respectively. Based on the above analysis, it can be con-

cluded that the proposed lion-swarm-optimization-based adaptive maximum correntropy filter exhibits strong robustness in the presence of measurement faults.

Table 1. Comparison of RMSE under faulty areas.

Method	Zone 1	Zone 2	Zone 3
EKF	1.85	2.54	2.37
MCRF (KB = 10)	1.84	2.45	2.14
MCRF (KB = 5)	1.79	2.19	1.49
MCRF (KB = 3)	1.69	1.65	1.33
AMCRF	1.50	1.45	1.51

5.3. Ramp Faults

To evaluate the robustness of the proposed algorithm under ramp fault conditions, a ramp fault with a rate of 0.5 m/s was injected into the pseudorange measurements of satellite PRN11 during the time interval from 201 s to 300 s, lasting for 100 s. Figure 8 presents the variation in horizontal positioning errors computed by different methods. Within the fault period, each method exhibited significantly different sensitivity to the ramp fault.

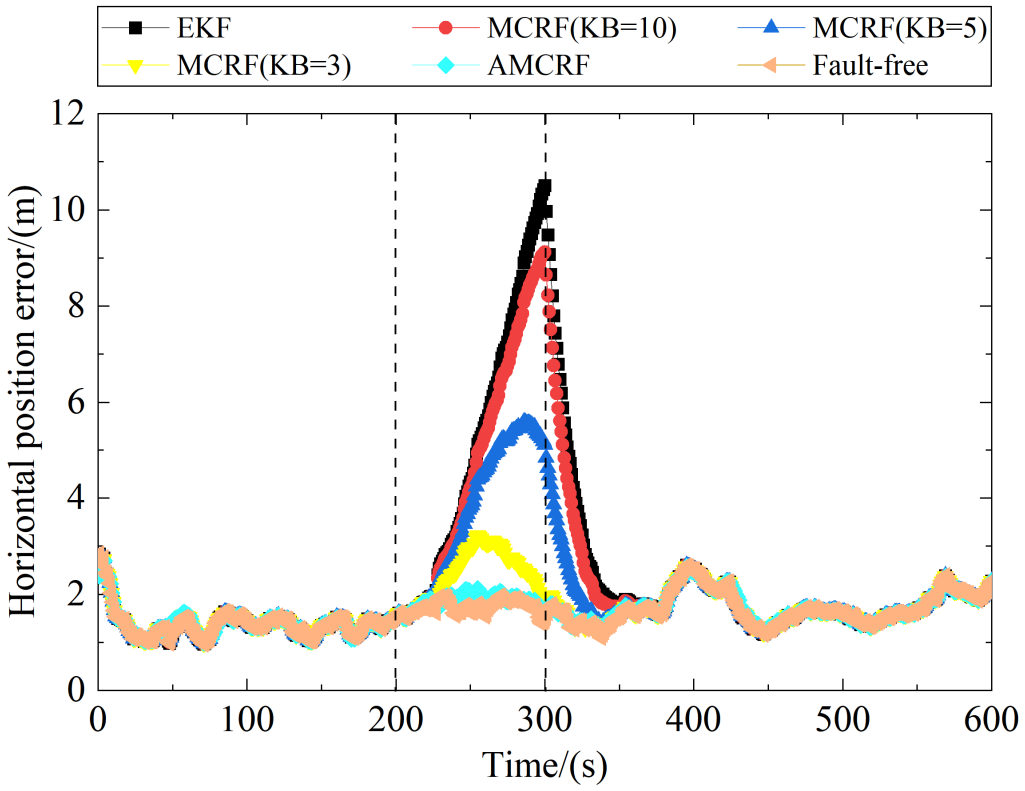

Figure 8. Robustness comparison under ramp faults.

The EKF showed the highest sensitivity, with positioning accuracy degrading continuously as the ramp fault increased, leading to a maximum horizontal positioning error of 10.5 m. In comparison, the three fixed-bandwidth MCRF variants demonstrated varying degrees of improvement. When the kernel bandwidth was set to 10, the maximum positioning error reached 9.12 m, which remained relatively close to that of the EKF. As the kernel bandwidth decreased, the positioning error also decreased. With kernel bandwidths of 5 and 3, the maximum errors were reduced to 5.59 m and 3.22 m, respectively. These results indicate that the fault suppression capability of MCRF depends on the choice of

kernel bandwidth, and selecting an appropriate bandwidth is critical to ensuring robust filtering performance.

Compared with MCRF, the AMCRF method achieved the best estimation performance, with a maximum positioning error of only 2.11 m. The error variation during the fault period remained relatively stable, demonstrating the strong fault tolerance of the proposed algorithm. Figure 9 further illustrates the dynamic adaptation of kernel bandwidths for each satellite within AMCRF. By allowing kernel bandwidths to vary based on measurement quality, the proposed method significantly enhances the overall robustness of the filtering process.

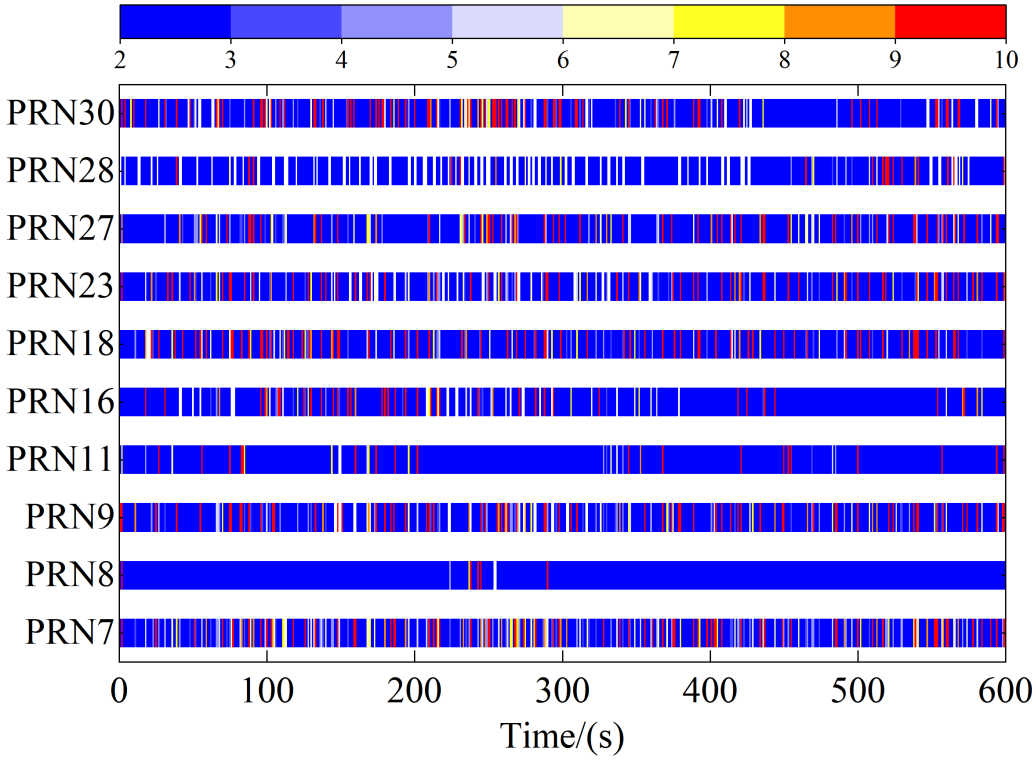

Figure 9. Variation of kernel bandwidths in AMCRF under ramp faults.

To quantitatively assess the positioning performance of the proposed algorithm, Figure 10 summarizes the maximum positioning error and RMSE obtained using different methods under the ramp fault scenario. Among all evaluated methods, AMCRF achieved the lowest RMSE, with a value of only 1.85 m. Compared with the EKF and the MCRF employing fixed kernel bandwidths of 10, 5, and 3, the RMSE of AMCRF were reduced by 67.7%, 64.9%, 53.3%, and 24.2%, respectively. Overall, the analysis demonstrates that the proposed AMCRF can effectively reduce the influence of step and ramp faults on state estimation, significantly improving the positioning accuracy.

5.4. Discussion

Compared with the studies reviewed in the Introduction, the proposed AMCRF primarily advances the state of the art in the following aspects. First, unlike conventional fault detection and exclusion methods, AMCRF does not require the explicit identification and removal of faulty measurements. Instead, it suppresses the influence of abnormal pseudorange observations during the filtering process by reconstructing the measurement noise covariance using the maximum correntropy criterion. This feature is beneficial for railway positioning scenarios with limited satellite visibility, where excluding measurements may weaken the satellite geometry and degrade positioning accuracy. Second, compared

with conventional robust filtering methods based on loss functions, AMCRF exploits the maximum correntropy criterion to enhance robustness against non-Gaussian measurement faults. Third, in contrast to existing MCC-based filters, which generally employ a fixed kernel bandwidth, AMCRF introduces a lion-swarm-optimisation-based adaptive bandwidth selection strategy. The kernel bandwidths are dynamically adjusted according to the measurement quality of each observed satellite, enabling the filter to adapt to time-varying measurement quality and varying fault magnitudes.

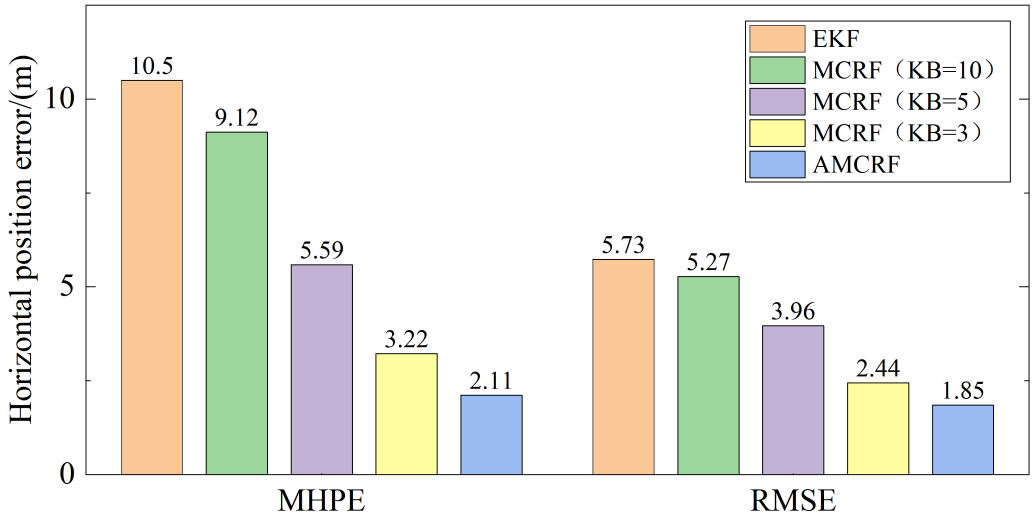

Figure 10. Comparison of positioning performance under ramp faulty areas.

Nevertheless, the proposed AMCRF still has several limitations. First, the experimental validation was conducted using data from the Qinghai–Tibet Railway under relatively good satellite visibility conditions. Further field tests are required in more challenging railway environments, such as mountainous valleys, dense urban areas, and severe multipath scenarios. Second, the present study mainly considers single-satellite step and ramp faults injected into pseudorange measurements. More complex fault scenarios, including simultaneous multi-satellite faults and INS sensor anomalies, should be further investigated.

6. Conclusions

This paper introduced an adaptive maximum correntropy robust filter that integrates the maximum correntropy criterion with a dynamic kernel bandwidth optimization strategy. By employing lion swarm optimization to adaptively tune kernel bandwidths, the algorithm effectively mitigates the impact of measurement faults. Experimental validation on the Qinghai–Tibet Railway confirmed that AMCRF consistently outperforms the conventional EKF and fixed-bandwidth MCRF methods under both step and ramp fault conditions. Notably, the algorithm maintained positioning errors at levels close to those observed under fault-free scenarios.

It should be noted that the present validation was mainly conducted under relatively favourable satellite visibility conditions. Therefore, further field validation is required to assess the performance of the proposed method in more challenging railway environments, such as severe multipath scenarios, mountainous valleys, and dense urban areas. In addition to environmental validation, future work will also consider more complex fault conditions, including simultaneous multi-satellite faults and INS sensor anomalies.

Author Contributions: Conceptualization, W.W. and C.P.; methodology, W.W. and S.S.; validation: C.P. and D.X.; resources: D.X.; data curation: W.W.; writing—original draft preparation, W.W. and C.P.; writing—review and editing, W.W. and C.P.; visualization, W.W.; supervision, D.X.; project

administration, W.W. and D.X.; funding acquisition, W.W. and D.X. All authors have read and agreed to the published version of the manuscript.

Funding: This research was supported by the China Academy of Railway Sciences Group Co., Ltd. Research Project (2024YJ087).

Data Availability Statement: Data will be made available on request.

Conflicts of Interest: Authors Weishu Wang, Shanyi Song and Dacheng Xu were employed by the company China Academy of Railway Sciences Corporation Limited. The remaining author declares that the research was conducted in the absence of any commercial or financial relationships that could be construed as a potential conflict of interest.

References

1. Peng, C.; Shangguan, W.; Wang, Z.; Peng, J.; Chai, L.; Xing, Y.; Cai, B. Reliability assessment of urban rail transit vehicle on-board controller with multi-component failure dependence based on R-vine-copula. *Reliab. Eng. Syst. Saf.* **2025**, *257*, 110795.
2. Fu, J.; Wang, Y.; Zhu, L.; Yu, Z.; Guo, B. Railway-Oriented Train Self-Localization Based on Visual Place Recognition. *Eng. Res. Express* **2026**, *8*, 095347.
3. Otegui, J.; Bahillo, A.; Lopetegi, I.; Díez, L.E. A survey of train positioning solutions. *IEEE Sens. J.* **2017**, *17*, 6788–6797. [CrossRef]
4. Gurník, P. Next generation train control (NGTC): More effective railways through the convergence of main-line and urban train control systems. *Transp. Res. Procedia* **2016**, *14*, 1855–1864. [CrossRef]
5. Betts, K.M.; Mitchell, T.J.; Reed, D.L.; Sloat, S.; Stranghoener, D.P.; Wetherbee, J.D. Development and operational testing of a sub-meter Positive Train Location system. In Proceedings of the 2014 IEEE/ION Position, Location and Navigation Symposium–PLANS, Monterey, CA, USA, 5–8 May 2014; pp. 452–461.
6. Cai, B.; Liu, J.; Dong, X.; Liu, J. Study on key technologies of GNSS-based train state perception for train-centric railway signaling. *High-Speed Railw.* **2023**, *1*, 47–55.
7. Stallo, C.; Neri, A.; Salvatori, P.; Coluccia, A.; Capua, R.; Olivieri, G.; Rispoli, F. GNSS-based location determination system architecture for railway performance assessment in presence of local effects. In Proceedings of the 2018 IEEE/ION Position, Location and Navigation Symposium, Monterey, CA, USA, 23–26 April 2018; pp. 374–381.
8. Mikhaylov, D.; Amatetti, C.; Polonelli, T.; Masina, E.; Campana, R.; Berszin, K.; Benini, L. Toward the future generation of railway localization exploiting RTK and GNSS. *IEEE Trans. Instrum. Meas.* **2023**, *72*, 1–10. [CrossRef]
9. Dai, X.; Song, W.; Wang, Y.; Xu, Y.; Lou, Y.; Tang, W. Lidar–inertial integration for rail vehicle localization and mapping in tunnels. *IEEE Sens. J.* **2023**, *23*, 17426–17438.
10. Lian, L.; Qin, Y.; Cao, Z.; Gao, Y.; Bai, J.; Ge, X.; Guo, B. A continuous autonomous train positioning method using stereo vision and object tracking. *IEEE Intell. Transp. Syst. Mag.* **2024**, *17*, 6–22. [CrossRef]
11. Heirich, O. Bayesian train localization with particle filter, loosely coupled GNSS, IMU, and a track map. *J. Sens.* **2016**, *2016*, 2672640. [CrossRef]
12. Jiang, W.; Chen, S.; Cai, B.; Wang, J.; ShangGuan, W.; Rizos, C. A multi-sensor positioning method-based train localization system for low density line. *IEEE Trans. Veh. Technol.* **2018**, *67*, 10425–10437.
13. Wang, D.; Shi, X.; Zhang, H.; Huo, J.; Cai, C. Visual landmark-aided LiDAR-inertial odometry for rail vehicle. *IEEE Sens. J.* **2024**, *24*, 27653–27665.
14. Wang, Z.; Yu, G.; Zhou, B.; Wang, P.; Wu, X. A train positioning method based on vision and millimeter-wave radar data fusion. *IEEE Trans. Intell. Transp. Syst.* **2021**, *23*, 4603–4613. [CrossRef]
15. Neri, A.; Battisti, F.; Baldoni, S.; Brizzi, M.; Pallotta, L.; Ruggeri, A.; Lauro, G. High accuracy high integrity train positioning based on GNSS and image processing integration. In Proceedings of the 34th International Technical Meeting of the Satellite Division of The Institute of Navigation, St. Louis, MO, USA, 20–24 September 2021; pp. 2670–2680.
16. Otegui, J.; Bahillo, A.; Lopetegi, I.; Díez, L.E. Evaluation of experimental GNSS and 10-DOF MEMS IMU measurements for train positioning. *IEEE Trans. Instrum. Meas.* **2018**, *68*, 269–279. [CrossRef]
17. Zhao, H.; Yang, Z. A novel fault detection and exclusion method for applying low-cost INS/GNSS integrated navigation system in urban environments. *IEEE Trans. Intell. Transp. Syst.* **2024**, *26*, 143–156.
18. Peng, C.; Peng, J.; Wang, Z.; Wang, Z.; Chen, J.; Xuan, J.; Shi, T. Adaptive fault diagnosis of railway vehicle on-board controller with large language models. *Appl. Soft Comput.* **2025**, *185*, 113919. [CrossRef]
19. Hu, X.; Zhang, K.; Huang, Y.; Cao, J.; Peng, D.; Chen, Z.; Tang, T. RRDNet: Robust Fault Diagnosis of Railway Switch Machines under Imperfect Sensing. *IEEE Trans. Instrum. Meas.* **2026**, *75*, 2507215. [CrossRef]
20. He, C.; Shi, H.; Liao, J.X.; Liu, B.; Liu, Q.; Li, J.; Yu, Z. Prior knowledge-embedded first-layer interpretable paradigm for rail transit vehicle human–computer collaboration fault monitoring. *J. Ind. Inf. Integr.* **2026**, *51*, 101068.

21. Lee, Y.C. Analysis of range and position comparison methods as a means to provide GPS integrity in the user receiver. In Proceedings of the 42nd Annual Meeting of the Institute of Navigation, Seattle, WA, USA, 24–26 June 1986; pp. 1–4.
22. Kuusniemi, H.; Lachapelle, G. GNSS signal reliability testing in urban and indoor environments. In Proceedings of the ION National Technical Meeting, San Diego, CA, USA, 26–28 January 2004; pp. 210–224.
23. Brown, R.G.; McBurney, P.W. Self-contained GPS integrity check using maximum solution separation. *Navigation* **1988**, *35*, 41–53. [CrossRef]
24. Zhang, P.; Chen, P.; Song, D.; Fan, G. Research on GNSS receiver autonomous integrity monitoring method based on M-estimation. *Math. Probl. Eng.* **2018**, *2018*, 2563202. [CrossRef]
25. Zhu, N.; Betaille, D.; Marais, J.; Berbineau, M. GNSS integrity enhancement for urban transport applications by error characterization and fault detection and exclusion. In *Géolocalisation et Navigation dans l'Espace et le Temps, Journées Scientifiques*; URSI: Paris, France, 2018; p. 11.
26. Bhatti, U.I.; Ochieng, W.Y.; Feng, S. Integrity of an integrated GPS/INS system in the presence of slowly growing errors. Part I: A critical review. *GPS Solut.* **2007**, *11*, 173–181.
27. Zhong, L.; Liu, J.; Li, R.; Wang, R. Approach for detecting soft faults in GPS/INS integrated navigation based on LS-SVM and AIME. *J. Navig.* **2017**, *70*, 561–579.
28. Al Hage, J.; El Najjar, M.E.B. Improved outdoor localization based on weighted Kullback-Leibler divergence for measurements diagnosis. *IEEE Intell. Transp. Syst. Mag.* **2018**, *12*, 41–56. [CrossRef]
29. Guo, B.; Li, W.; Hu, G.; Zhu, X. Mahalanobis distance-based fading cubature Kalman filter with augmented mechanism for hypersonic vehicle INS/CNS autonomous integration. *Chin. J. Aeronaut.* **2022**, *35*, 114–128.
30. Marais, J.; Nahimana, D.F.; Viandier, N.; Duflos, E. GNSS accuracy enhancement based on pseudorange error estimation in an urban propagation environment. *Expert Syst. Appl.* **2013**, *40*, 5956–5964.
31. Ge, Y.; Yuan, Y.; Jia, N. More efficient methods among commonly used robust estimation methods for GPS coordinate transformation. *Surv. Rev.* **2013**, *45*, 229–234. [CrossRef]
32. Zhao, J.; Sun, W.; Ding, W.; Li, Y.; Sun, P.; Sun, P. Vehicle cooperative positioning with tightly coupled GNSS/INS/UWB integration based on improved multiple fading factors and adaptive cost function. *IEEE Trans. Intell. Transp. Syst.* **2025**, *26*, 9740–9754.
33. Chen, B.; Liu, X.; Zhao, H.; Principe, J.C. Maximum correntropy Kalman filter. *Automatica* **2017**, *76*, 70–77. [CrossRef]
34. Fan, X.; Wang, G.; Han, J.; Wang, Y. Interacting multiple model based on maximum correntropy Kalman filter. *IEEE Trans. Circuits Syst. II Express Briefs* **2021**, *68*, 3017–3021. [CrossRef]
35. Liu, X.; Liu, X.; Yang, Y.; Guo, Y.; Zhang, W. Variational Bayesian-based robust cubature Kalman filter with application on SINS/GPS integrated navigation system. *IEEE Sens. J.* **2021**, *22*, 489–500.
36. Peng, C.; Shangguan, W.; Peng, J.; Wang, Z.; Chai, L.; Cai, B.; Xing, Y. Multi-objective preventive maintenance strategy and optimization considering unavailability and cost: A case study on VOBC. *Alex. Eng. J.* **2024**, *105*, 567–577. [CrossRef]
37. Peng, C.; Shangguan, W.; Cai, B.; Chen, B. Multi-objective optimal maintenance strategy considering imperfect preventive maintenance: A case study on railway VOBC. *Proc. Inst. Mech. Eng. Part O J. Risk Reliab.* **2024**, *238*, 740–753.
38. Zhu, N. GNSS Propagation Channel Modeling in Constrained Environments: Contribution to the Improvement of the Geolocation Service Quality. Ph.D. Thesis, Université de Lille, Lille, France, 2018.
39. Wang, Y.; Liu, D. Maximum correntropy cubature Kalman filter and smoother for continuous-discrete nonlinear systems with non-Gaussian noises. *ISA Trans.* **2023**, *137*, 436–445. [PubMed]